

# Observation of Phase Controllable Majorana-like Bound States in Metamaterial-based Kitaev Chain Analogues

Kai Qian,<sup>1,\*</sup> David J. Apigo,<sup>1</sup> Karmela Padavić,<sup>2,†</sup>  
Keun Hyuk Ahn,<sup>1,‡</sup> Smitha Vishveshwara,<sup>2</sup> and Camelia Prodan<sup>1,§</sup>

<sup>1</sup>*Department of Physics, New Jersey Institute of Technology, Newark, New Jersey, 07102, USA*

<sup>2</sup>*Department of Physics, University of Illinois at Urbana-Champaign, Urbana, Illinois, 61801, USA*

We experimentally demonstrate that Majorana-like bound states (MLBSs) can occur in quasi-one-dimensional metamaterials, analogous to Majorana zero modes (MZM) in the Kitaev chain. In a mechanical spinner ladder system, we observe a topological phase transition and spectral-gap-protected edge MLBSs. We characterize the decaying and oscillatory nature of these MLBS pairs and their phase-dependent hybridization. It is shown that the hybridization can be tuned to yield the analogue of parity switching in MZMs, a key element of topological qubits. We find strong agreements with theory.

In the past decade, the rich cross-fertilization of ideas between the studies of electronic and mechanical systems has led to the discovery of exciting new states of matter, including physical behaviors driven by topology [1–6]. For example, a Chern insulator with one-way edge modes was demonstrated using an array of gyroscopes [7, 8]. Among electronic materials, topological superconductors have gained prominence as candidates for hosting Majorana zero modes (MZMs), which are potential building blocks of fault tolerant quantum computing [9–20]. The Kitaev chain [21], consisting of electrons hopping on a lattice subject to  $p$ -wave pairing, provides an excellent prototype for realizing MZMs as topologically protected edge states [22–25]. Remarkably, these modes have remained elusive in solid state systems despite tremendous efforts [26–33]. Nevertheless, MZMs have continued to inspire experimental realizations of analogous modes in other systems [34, 35], including metamaterials. Even key traits for error-free MZM qubits, like non-Abelian braiding, have recently been proposed in classical metamaterials systems [36].

In this Letter, we present a mechanical metamaterial ladder system made of magnetically coupled spinners, and demonstrate that it closely parallels several salient features of the Kitaev chain, including distinct presence of Majorana-like bound states (MLBSs). In previous work by two of the current authors and collaborators [37], it was shown that the phase diagram, mode spectrum, and associated wavefunctions of the Kitaev chain could be mapped to a system of two coupled Su-Schrieffer-Heeger (SSH) chains [38], characterized by alternating bond strengths schematically shown in Fig. 1(b). A significant benefit of this mapping is that the SSH ladder system can be realized in a variety of systems whether they be bosonic, fermionic or involve classical metamaterials. Although MLBSs in these systems may not be exactly equivalent to MZMs, they are topologically protected by spectral gaps. In a coupled split-ring-resonator system, Guo *et al.* [39] observed one such metamaterial realization of MLBSs and a topological phase transition

up to finite size effects. Here, our work on the spinner system explores a topological phase transition for sufficiently long ladders, thus eliminating size effects, and the properties of the MLBS at the edges that were theoretically predicted [37, 40–42] but never fully realized.

In what follows, we demonstrate the remarkable analogues to Kitaev chain features in metamaterials, including spectral characteristics of topological and nontopological phases, oscillatory, decaying MZM wavefunctions, and switching behavior in fermion parity, which forms the basis of MZM qubits. The Kitaev chain is described by the Hamiltonian [21, 37],

$$H_K = \frac{1}{2i} \sum_n (\omega - \Delta) a_n b_{n+1} + (\omega + \Delta) a_{n+1} b_n + \mu a_n b_n, \quad (1)$$

where  $a_n$  and  $b_n$  are the Majorana operators,  $\omega$  the nearest neighbor electron hopping amplitude,  $\Delta$  the  $p$ -wave superconducting order parameter, and  $\mu$  the chemical potential. One of the two topological gapped phases, hosting mid-gap MZMs, occurs at  $|\mu| < 2|\omega|$  and  $\Delta > 0$  and the other at  $|\mu| < 2|\omega|$  and  $\Delta < 0$ , while nontopological gapped phases arise at  $|\mu| > 2|\omega|$ .

Mechanical systems of magnetically coupled spinners [43–46] have recently been used to simulate a number of electronic tight-binding Hamiltonians. The spinner ladder system pictured in Fig. 1(a) shows the metamaterial analogue of the SSH ladder in Fig. 1(b). Here the electron hopping translates to the interspinner magnetic interaction controlled by the distance between magnets, and the electronic eigenstate energy maps to the frequency squared ( $f^2$ ) for the spinner normal modes. With magnets attached to selected spinner arms, nearest-neighbors connected by the red, blue, and green lines in Fig. 1(b) have attractive interactions, parameterized by normalized positive constants  $\beta_r$ ,  $\beta_b$ , and  $\beta_g$ , respectively. As marked by solid circles and open triangles in Fig. 1(b), the system is bipartite, and the rotations of the spinners are represented by  $\theta_n$  and  $\varphi_n$  with  $n = 1, \dots, N$  within each sublattice for the system of length  $N$ . One of the spinners is driven externally, and attached accelerometers monitor oscillations. De-

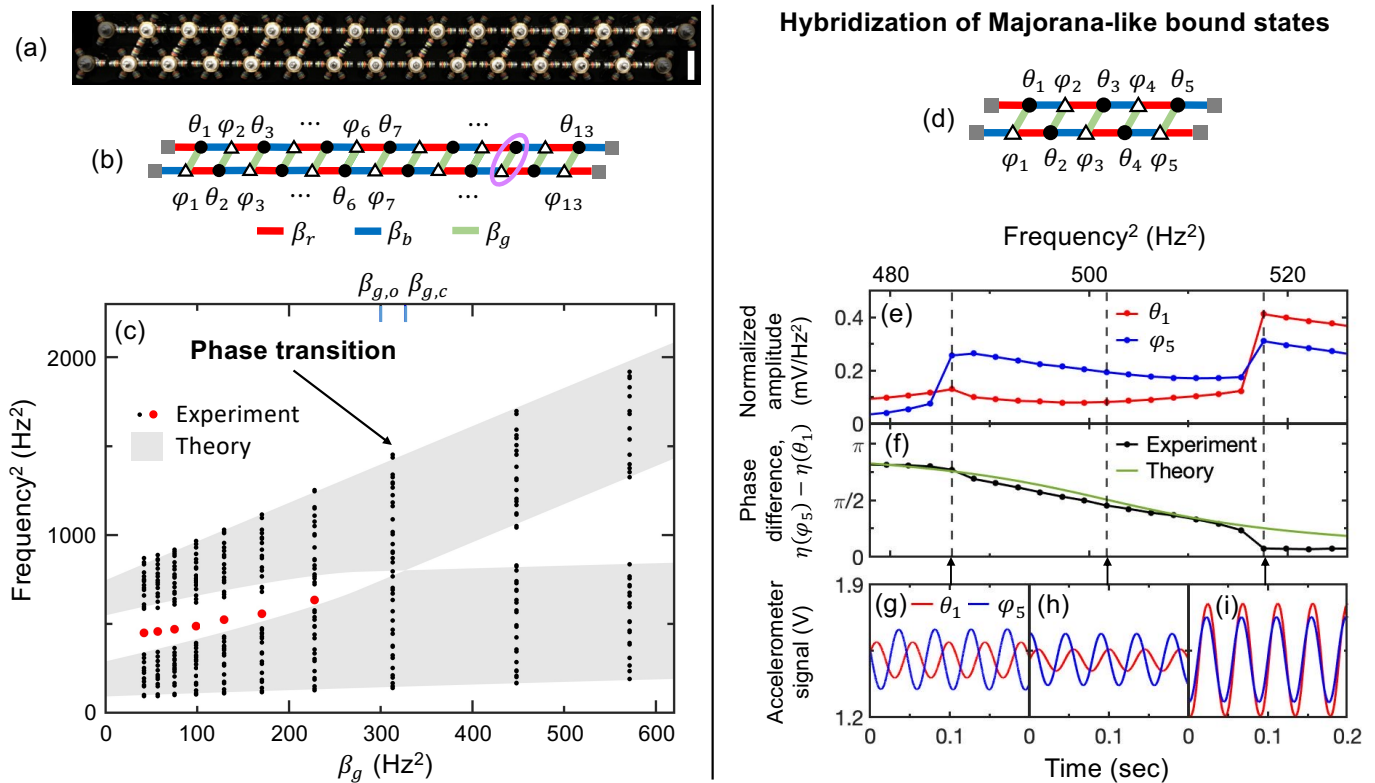


FIG. 1. Phase transition for a long ladder system (left) and phase-controllable hybridized MLBSs for a short ladder system (right). (a) Picture of the experimental setup for a system of length  $N=13$ . Rotatable spinners and magnetically coupled arms are highlighted and fixed spinners and arms without magnets are shaded. The scale on the right is 5.0 cm. (b) Schematic diagram for the SSH ladder system pictured in (a). The rotatable spinners are represented by black circles ( $\theta_n$ ) and open triangles ( $\varphi_n$ ), and the fixed spinners by gray squares. The purple ellipse shows the unit cell. The red and blue lines denote the *intrachain* coupling  $\beta_r = 230 \text{ Hz}^2$  and  $\beta_b = 100 \text{ Hz}^2$ , respectively, and the green line the *interchain* coupling  $\beta_g$ . (c) Topological phase transition for the long  $N=13$  system signaled by the emergence of mid-gap MLBSs. The measured frequency squared ( $f^2$ ) for normal mode versus  $\beta_g$  is shown for various interchain coupling  $\beta_g$ . The red dots correspond to the mid-gap MLBSs, while the black dots bulk states. The gray areas represent the theoretical bulk bands in the limit of the infinitely long system. The two critical interchain couplings,  $\beta_{g,c} = 330 \text{ Hz}^2$  for the phase transition and  $\beta_{g,o} = 300 \text{ Hz}^2$  for oscillatory MLBSs, are marked on the top axis. (d) Schematic diagram for the short  $N=5$  system. (e) Spectra obtained by actuating  $\theta_1$  spinner and measuring at  $\theta_1$  and  $\varphi_5$  spinners, shown in red and blue dots, respectively, within the bulk gap for the topological phase with  $\beta_g = 100 \text{ Hz}^2$  and  $\beta_r$  and  $\beta_b$  identical to those for (c). A single degenerate MLBS peak in (c) is split into two MLBS peaks due to the enhanced hybridization. (f) Phase difference between the  $\varphi_5$  and  $\theta_1$  spinners,  $\eta(\varphi_5) - \eta(\theta_1)$ , versus  $f^2$ , revealing phase controllable MLBSs. (g), (h) and (i): Three examples of the accelerometer signals, proportional to the rotation angles, versus time for lower MLBS, in-between, and upper MLBS, as marked by arrows. The red and blue lines represent the oscillations of the  $\theta_1$  and  $\varphi_5$  spinners. (See Supplemental Material [47] for typical spectra, gap versus  $\beta_g$ , and videos for modes.)

tails of the setup are provided in Supplemental Material [47] and Refs. [43–45]. The normalized Lagrangian for the spinner system is  $L = T - U_1 - U_2$ , where  $T = \sum_{n=1}^N (\dot{\theta}_n^2 + \dot{\varphi}_n^2) / 8\pi^2$  is the normalized kinetic energy, and  $U_1 = -\sum_{n=1}^N \alpha (\theta_n^2 + \varphi_n^2) / 2$  with a positive coefficient  $\alpha$  and

$$U_2 = -\sum_n \beta_b \theta_n \varphi_{n+1} + \beta_r \theta_{n+1} \varphi_n + \beta_g \theta_n \varphi_n \quad (2)$$

represent the normalized potential energy. While the term  $U_1$  shifts the spectrum by a constant, the term  $U_2$  has the form identical to  $H_K$  in Eq. (1), depicted by the mapping shown in Table I. This mapping allows us to explore the analogy between the metamaterials and elec-

tronic systems through direct excitations of spinners, as shown in videos in Supplemental Material [47].

In long ladders, we observe a clear phase transition between nontopological and topological phases characterized by mid-gap MLBS as a function of the interaction between SSH chains, which is analogous to the chemical potential in the Kitaev chain. Figure 1(c) shows  $f^2$  for normal modes versus the interchain coupling  $\beta_g$  for the  $N=13$  spinner systems [see Figs. 1(a) and 1(b)] with intrachain couplings  $\beta_r = 230 \text{ Hz}^2$  and  $\beta_b = 100 \text{ Hz}^2$ . Bulk modes, shown as black dots, are identified from the resonant oscillations of spinners near the center of the system. In contrast, the red dot in the spectrum corre-

SSH spinner ladder system	$\theta_n$	$\varphi_n$	$\beta_b$	$\beta_r$	$\beta_g$
Electronic Kitaev chain	$a_n$	$b_n$	$\omega - \Delta$	$\omega + \Delta$	$\mu$

TABLE I. Mapping between the parameters of the SSH spinner ladder system [Eq. (2)] and the electronic Kitaev chain [Eq. (1)]. For the spinner system, the  $\theta_n$  and  $\varphi_n$  represent the rotation angles of the spinners, the  $\beta_b$  and  $\beta_r$  the *intra-chain* interactions, and the  $\beta_g$  the *interchain* interaction, as shown in Figs. 1(b) and 1(d). For the Kitaev chain,  $a_n$  and  $b_n$  are the Majorana operators,  $\omega$  the nearest neighbor electron hopping amplitude,  $\Delta$  the *p*-wave superconducting order parameter, and  $\mu$  the chemical potential [37].

sponds to the MLBS at one of the system's ends, and is prominently identified from measurement of the  $\theta_1$  spinner. We expect another MLBS mode at the other end at the same frequency. (See Supplemental Material for typical spectra [47].) Starting from large interchain coupling  $\beta_g$ , the gap in the bulk spectra rapidly narrows as  $\beta_g$  decreases, and closes when  $\beta_g \approx 310 \text{ Hz}^2$ , consistent with the theoretical phase boundary  $\beta_{g,c} = \beta_r + \beta_b = 330 \text{ Hz}^2$  (see the top axis). As  $\beta_g$  decreases further, the gap reopens but with a distinct mid-gap mode, which marks the topological phase transition. Bulk bands fall within the theoretically predicted range for the infinitely long ladder system [37] shown in gray. We conclude that the  $N=13$  spinner system realizes the long ladder limit, thus expanding on the results in Ref. [39], where finite size effects presented more of a limitation. (See Supplemental Material for gap versus  $\beta_g$  and theoretical ranges for bulk bands [47].)

Realizing the short topological systems, we find that MLBSs from the two ends overlap, and therefore the degenerate end modes of the long limit hybridize and split in frequency, in close analogy to hybridization of MZM wavefunctions. To first order, the split modes correspond to symmetric and antisymmetric combinations of the MLBS up to a tunable relative phase. For the infinitely long topological system, theory predicts that MLBSs reside on the  $\theta_n$ -sublattice at the left edge and on the  $\varphi_n$ -sublattice at the right edge if  $\beta_r > \beta_b$  (as in all cases in this Letter). For the short topological system with  $N=5$ , schematically shown in Fig. 1(d), the hybridization and splitting is evident in Fig. 1(e), where the normalized amplitudes measured at the  $\theta_1$  [ $\varphi_5$ ] spinner are plotted with respect to  $f^2$  within the gap in red [blue] dots. To reveal the impact of the significant overlap of the two peaks, we measure the angles,  $\theta_1$  and  $\varphi_5$ , versus time at three frequencies indicated by the dashed lines in Fig. 1(e), that is, the lower and upper MLBS frequencies, and a frequency in between, as shown in Figs. 1(g), 1(i), and 1(h), respectively. The phase differences between  $\varphi_5$  and  $\theta_1$ ,  $\eta(\varphi_5) - \eta(\theta_1)$ , are  $0.77\pi$  and  $0.07\pi$  for the lower and upper MLBSs, respectively. In being close to  $\pi$  or 0, they mimic the theoretical results for an ideal system without damping, that is, odd or even symmetry.

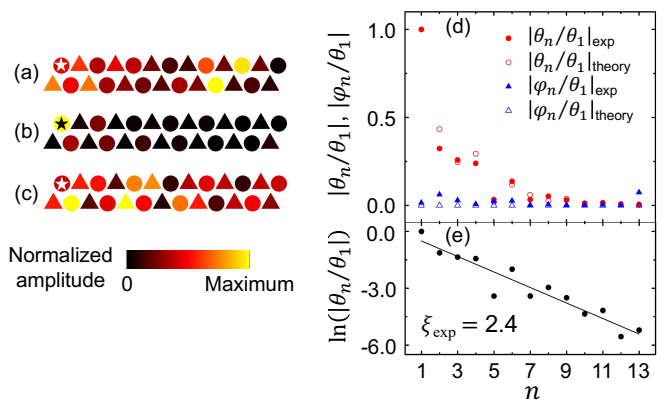


FIG. 2. Localization of the MLBS for a system with  $N = 13$  and  $\beta_g = 100 \text{ Hz}^2$ , a case in Fig. 1(c). (a)-(c) Rotational oscillation amplitudes of spinners measured for (a) an upper bulk mode, (b) a mid-gap MLBS, and (c) a lower bulk mode (See Supplemental Material [47] for videos). The color represents the rotational oscillation amplitude of each spinner. The stars mark the actuated spinners. (d) Normalized rotational oscillation amplitudes,  $|\theta_n/\theta_1|$  (red circles) and  $|\varphi_n/\theta_1|$  (blue triangles), versus  $n$ . The solid and open symbols represent the experimental and theoretical results. (e) Symbols: semilogarithmic plot of  $\ln|\theta_n/\theta_1|$  versus  $n$  for the experiments. Line: linear fit giving a localization length  $\xi_{\text{exp}} = 2.4$ , consistent with the theory.

Similarly, for a series of frequencies in the gap, the relative phase  $\eta(\varphi_5) - \eta(\theta_1)$  is plotted as dots in Fig. 1(f). It shows a continuous change of the phase difference, in agreement with theoretical results for a damped system shown in green line. Here, we emphasize that the tunability of the relative phase in our system may have future applications in mechanical memories [48].

Importantly, MLBSs are not only bipartite and decaying, but also characterized by spatial oscillations. For instance, for the topological  $N=13$  system with  $\beta_g = 100 \text{ Hz}^2$  in Fig. 1(c), rotational oscillation amplitudes of the spinners for the MLBS are displayed in colors in Fig. 2(b). Here, it is revealed that the MLBS resides mostly on the  $\theta_n$  sites (circles) near the left edge, unlike typical bulk modes shown in Figs. 2(a) and 2(c) (See Supplemental Material for videos [47].). The detailed structure of the MLBS is seen in Fig. 2(d), where the normalized amplitude for the  $\theta_n$  ( $|\theta_n/\theta_1|$ , red solid circles) is large near the left edge, while amplitude for the  $\varphi_n$  ( $|\varphi_n/\theta_1|$ , blue solid triangles) is negligible. These results qualitatively agree with Ref. [39], but with an important difference: in our system the decaying amplitude *oscillates*. Moreover, this oscillation rather successfully matches theoretical predictions [42] and is the first to realize them. For MZMs in the Kitaev chain, theory [42] predicts such oscillatory wavefunctions within a circle in the phase diagram set by  $\mu^2 + (2\Delta)^2 < (2\omega)^2$ . Translated to the spinner system, the spatial profile of the MLBS localized at the left edge is given by  $\theta_n = A \exp(-n/\xi_{\text{theory}}) \cos(B + 2n\pi/\lambda)$

if  $\beta_g < \beta_{g,o}$ , where  $\xi_{\text{theory}} = 2[\ln(\beta_r/\beta_b)]^{-1}$  is the localization length,  $\lambda$ ,  $A$ , and  $B$  are constants, and  $\beta_{g,o} = 2\sqrt{\beta_b\beta_r}$  (see Supplemental Material for details [47]). For the system in Fig. 2,  $\beta_g = 100 \text{ Hz}^2$  is indeed less than  $\beta_{g,o} = 300 \text{ Hz}^2$  [see the top axis in Fig. 1(c)], and the theoretical results for the  $|\theta_n/\theta_1|$  and  $|\varphi_n/\theta_1|$  plotted in open symbols in Fig. 2(d) agree well with the experiments. Further, a linear fit of  $\ln|\theta_n/\theta_1|$  versus  $n$  for the experiments shown in Fig. 2(e) results in  $\xi_{\text{exp}} = 2.4$ , identical to the theoretical value  $\xi_{\text{theory}}$ . Strong agreement with the theory confirms that the spatial oscillation seen here is not due to disorder, but reflects the intrinsic nature of the MLBS spatial profiles, analogous to the oscillatory MZM wavefunctions.

The oscillatory behavior of the MLBSs significantly affects spectral features of the system. Most importantly, when their hybridization changes its sign, there is a switch between whether the symmetric or the antisymmetric combination corresponds to the lower frequency. In the MZM analogue, this behavior results in so-called parity switching [40–42, 49]. Here, consequences of the switch are rather profound: the two end MZMs form a Dirac fermionic state that can be occupied or unoccupied, essentially a topological qubit, thus giving the system odd or even parity. In other words, the sign of the hybridization determines ground state parity. To demonstrate the analogue of this switching in the topological spinner systems, we vary the length of the system,  $N=3, 4, \dots, 8$ , while keeping the interactions identical to Figs. 1(d)-1(i). Normalized amplitudes of the  $\varphi_N$  spinner (resulting from actuating the  $\theta_1$  spinner) versus  $f^2$  within the bulk gap are shown as *solid* symbols in Fig. 3(a). The split of the MLBSs, indicated by yellow areas in Fig. 3(a) and solid circles in Fig. 3(b), clearly oscillates as  $N$  increases, in agreement with theoretical results, shown as open circles in Fig. 3(b). Behavior of the spinner system analogous to parity switching is most evident in the phase difference between the  $\varphi_N$  and  $\theta_1$  spinner,  $\eta(\varphi_N) - \eta(\theta_1)$ , versus  $f^2$  shown as *open* symbols in Fig. 3(a). The phase difference changes approximately from  $\pi$  to 0 as the frequency increases for  $N=5$  and 8, but from 0 to  $-\pi$  for  $N=3, 4, 6$ , and 7. The observed switch in the phase difference for the upper MLBS is displayed in Fig. 3(b) using the background color for each  $N$ , that is, blue for  $\eta(\varphi_N) - \eta(\theta_1) \approx 0$  (even symmetry) and red for  $\pm\pi$  (odd). It agrees with the theory except for the  $N=4$  case (purple, odd from the experiments, but even from the theory) [42, 50]. The phase switching seen here may prove to be a consequential feature when it comes to designing MZM qubits, because it strengthens the proposal that the chemical potential be tuned to achieve exactly degenerate MZMs in finite Kitaev chains [40–42].

In conclusion, demonstrating the potentiality of research that connects electronic and metamaterial systems, we analyzed surprisingly close analogues of MZMs in Kitaev chains with MLBSs in spinner ladders. While

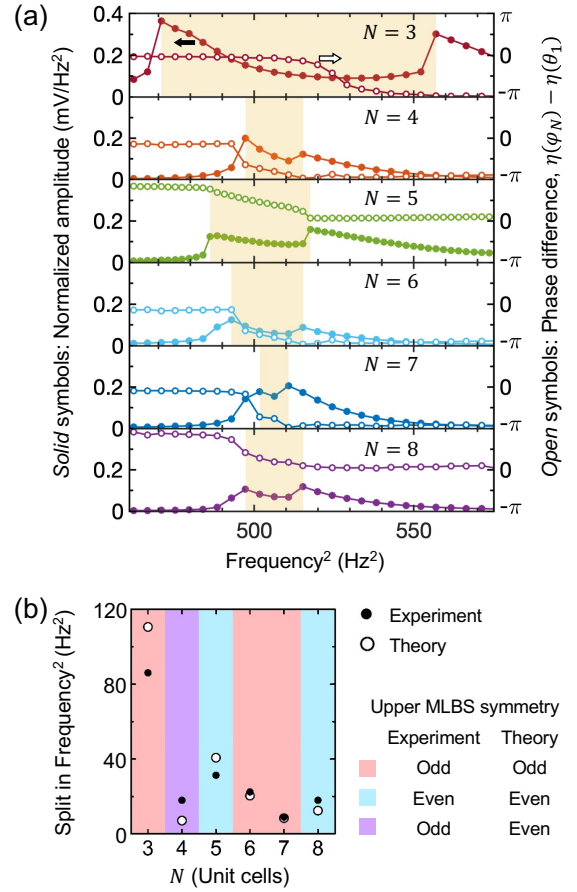


FIG. 3. Split oscillation and phase difference switching of the hybridized MLBSs as varying the length of the systems. (a) *Solid* symbols: Spectra of the topological systems for  $N = 3, 4, \dots, 8$ , obtained by actuating  $\theta_1$  and measuring at  $\varphi_N$  spinners for the frequencies within the bulk gap. The interactions are kept identical to those in Figs. 1(d)-1(i). The widths of the yellow areas represent the splits of the hybridized MLBSs. *Open* symbols: The corresponding phase differences,  $\eta(\varphi_N) - \eta(\theta_1)$ . (b) Symbols: Split between the hybridized MLBSs versus the length of the system,  $N$ , for the experiments (solid symbols) and the theory (open symbols). Background colors: Observed phase difference of the upper MLBS is shown in blue for close to 0 (even symmetry) and red for  $\pm\pi$  (odd), agreeing with the theory. A disagreement between theory and experiments occurs for  $N=4$  case, shown in purple, likely due to disorder in the experimental setup [50].

the degrees of freedom differ, our in-depth realization provides a well-controlled prototype for benchmarking any MZMs and Majorana-based qubits that may be discovered in the future [51]. Further, our studies signal promise for next-generation metamaterial applications, such as topological braiding of mid-gap states in the case of stacked SSH ladders [36]. From the metamaterials perspective, states like MLBSs that are protected by spectral gaps offer wide possibilities, such as mechanical memory and device applications.

K.Q. and C.P. acknowledge support from the W. M. Keck Foundation. C. P. acknowledges support from National Science Foundation (NSF Award 2131759). K.Q., K.H.A. and C.P. acknowledge support of NJIT Faculty Seed Grant. S.V. acknowledges support of the National Science Foundation and the Quantum Leap Challenge Institute for Hybrid Quantum Architectures and Networks (NSF Award 2016136).

---

\* Present address: Department of Mechanical Aerospace and Engineering, University of California San Diego, La Jolla, California 92093, USA

† Present address: Department of Science, Bard High School Early College, New York, New York 10002, USA

‡ kenahn@njit.edu

§ cprodan@njit.edu

- [1] E. Prodan and C. Prodan, Topological phonon modes and their role in dynamic instability of microtubules, *Phys. Rev. Lett.* **103**, 248101 (2009).
- [2] S. D. Huber, Topological mechanics, *Nature Phys.* **12**, 621 (2016).
- [3] C. L. Kane and T. C. Lubensky, Topological boundary modes in isostatic lattices, *Nature Phys.* **10**, 39 (2014).
- [4] B. G.-g. Chen, B. Liu, A. A. Evans, J. Paulose, I. Cohen, V. Vitelli, and C. D. Santangelo, Topological mechanics of origami and kirigami, *Phys. Rev. Lett.* **116**, 135501 (2016).
- [5] P. Gao, D. Torrent, F. Cervera, P. San-Jose, J. Sánchez-Dehesa, and J. Christensen, Majorana-like zero modes in Kekulé distorted sonic lattices, *Phys. Rev. Lett.* **123**, 196601 (2019).
- [6] B. G.-g. Chen, N. Upadhyaya, and V. Vitelli, Nonlinear conduction via solitons in a topological mechanical insulator, *Proc. Natl Acad. Sci. USA* **111**, 13004 (2014).
- [7] L. M. Nash, D. Kleckner, A. Read, V. Vitelli, A. M. Turner, and W. T. M. Irvine, Topological mechanics of gyroscopic metamaterials, *Proc. Natl Acad. Sci. USA* **112**, 14495 (2015).
- [8] P. Wang, L. Lu, and K. Bertoldi, Topological phononic crystals with one-way elastic edge waves, *Phys. Rev. Lett.* **115**, 104302 (2015).
- [9] E. Majorana, Teoria simmetrica dell'elettrone e del positrone, *E. Nuovo Cimento* **5**, 171 (1937).
- [10] A. Y. Kitaev, Fault-tolerant quantum computation by anyons, *Ann. Phys. (N.Y.)* **303**, 2 (2003).
- [11] C. Nayak, S. H. Simon, A. Stern, M. Freedman, and S. D. Sarma, Non-Abelian anyons and topological quantum computation, *Rev. Mod. Phys.* **80**, 1083 (2008)
- [12] F. Wilczek, Majorana returns, *Nature Phys.* **5**, 614 (2009).
- [13] R. M. Lutchyn, J. D. Sau, and S. D. Sarma, Majorana fermions and a topological phase transition in semiconductor-superconductor heterostructures, *Phys. Rev. Lett.* **105**, 077001 (2010).
- [14] Y. Oreg, G. Refael, and F. von Oppen, Helical liquids and Majorana bound states in quantum wires, *Phys. Rev. Lett.* **105**, 177002 (2010).
- [15] J. Alicea, New directions in the pursuit of Majorana fermions in solid state systems, *Rep. Prog. Phys.* **75**, 076501 (2012).
- [16] P. Hosur, P. Ghaemi, R. S. K. Mong, and A. Vishwanath, Majorana modes at the ends of superconductor vortices in doped topological insulators, *Phys. Rev. Lett.* **107**, 097001 (2011).
- [17] M. Leijnse and K. Flensberg, Introduction to topological superconductivity and Majorana fermions, *Semicond. Sci. Technol.* **27**, 124003 (2012).
- [18] J. C. Teo and T. L. Hughes, Existence of Majorana-fermion bound states on disclinations and the classification of topological crystalline superconductors in two dimensions, *Phys. Rev. Lett.* **111**, 047006 (2013).
- [19] S. Nadj-Perge, I. K. Drozdov, J. Li, H. Chen, S. Jeon, J. Seo, A. H. MacDonald, B. A. Bernevig, and A. Yazdani, Observation of Majorana fermions in ferromagnetic atomic chains on a superconductor, *Science* **346**, 602 (2014).
- [20] M. Sato and S. Fujimoto, Majorana fermions and topology in superconductors, *J. Phys. Soc. Jpn.* **85**, 072001 (2016).
- [21] A. Y. Kitaev, Unpaired Majorana fermions in quantum wires, *Phys. Usp.* **44**, 131 (2001).
- [22] J. Chubb, A. Eskandarian, and V. Harizanov, editors, *Logic and Algebraic Structures in Quantum Computing* (Cambridge University Press, Cambridge, 2016).
- [23] B. Lian, X. Q. Sun, A. Vaezi, X. L. Qi, and S. C. Zhang, Topological quantum computation based on chiral Majorana fermions, *Proc. Natl. Acad. Sci. U. S. A.* **115**, 10938 (2018).
- [24] R. Aguado and L. Kouwenhoven, Majorana qubits for topological quantum computing, *Phys. Today* **73**, 6, 44 (2020).
- [25] C. Tutschku, R. W. Reithaler, C. Lei, A. H. MacDonald, and E. M. Hankiewicz, Majorana-based quantum computing in nanowire devices, *Phys. Rev. B* **102**, 125407 (2020).
- [26] T. L. Hughes, Majorana fermions inch closer to reality, *Physics* **4**, 67 (2011).
- [27] V. Mourik, K. Zuo, S. M. Frolov, S. R. Plissard, E. P. A. M. Bakkers, and L. P. Kouwenhoven, Signatures of Majorana fermions in hybrid superconductor-semiconductor nanowire devices, *Science* **336**, 1003 (2012).
- [28] L. P. Rokhinson, X. Liu, and J. K. Furdyna, The fractional a.c. Josephson effect in a semiconductor-superconductor nanowire as a signature of Majorana particles, *Nat. Phys.* **8**, 795 (2012).
- [29] A. Das, Y. Ronen, Y. Most, Y. Oreg, M. Heiblum, and H. Shtrikman, Zero-bias peaks and splitting in an Al-InAs nanowire topological superconductor as a signature of Majorana fermions, *Nat. Phys.* **8**, 887 (2012).
- [30] S. M. Albrecht, A. P. Higginbotham, M. Madsen, F. Kuemmeth, T. S. Jespersen, J. Nygård, P. Krogstrup, and C. M. Marcus, Exponential protection of zero modes in Majorana islands, *Nature (London)* **531**, 206 (2016).
- [31] M. T. Deng, S. Vaitiekenas, E. B. Hansen, J. Danon, M. Leijnse, K. Flensberg, J. Nygård, P. Krogstrup, and C. M. Marcus, Majorana bound state in a coupled quantum-dot hybrid-nanowire system, *Science* **354**, 1557 (2016).
- [32] R. M. Lutchyn, E. P. A. M. Bakkers, L. P. Kouwenhoven, P. Krogstrup, C. M. Marcus and Y. Oreg, Majorana zero modes in superconductor-semiconductor heterostructures, *Nat. Rev. Mater.* **3**, 52 (2018).
- [33] Z. Wang, J. O. Rodriguez, L. Jiao, S. Howard, M. Graham, G. D. Gu, T. L. Hughes, D. K. Morr, and V. Mad-

- havan, Evidence for dispersing 1D Majorana channels in an iron-based superconductor, *Science* **367**, 104 (2020).
- [34] S. Vishveshwara and D. M. Weld,  $Z_2$  phases and Majorana spectroscopy in paired Bose-Hubbard chains, *Phys. Rev. A* **103**, L051301 (2021).
- [35] A. McDonald, T. Pereg-Barnea, and A. A. Clerk, Phase-dependent chiral transport and effective non-Hermitian dynamics in a bosonic Kitaev-Majorana chain, *Phys. Rev. X* **8**, 041031 (2018).
- [36] Y. Barlas and E. Prodan, Topological braiding of non-Abelian midgap defects in classical metamaterials, *Phys. Rev. Lett.* **124**, 146801 (2020).
- [37] K. Padavić, S. S. Hegde, W. DeGottardi, and S. Vishveshwara, Topological phases, edge modes, and the Hofstadter butterfly in coupled Su-Schrieffer-Heeger systems, *Phys. Rev. B* **98**, 024205 (2018).
- [38] W. P. Su, J. R. Schrieffer, and A. J. Heeger, Solitons in polyacetylene, *Phys. Rev. Lett.* **42**, 1698 (1979).
- [39] Z. Guo, J. Jiang, H. Jiang, J. Ren, and H. Chen, Observation of topological bound states in a double Su-Schrieffer-Heeger chain composed of split ring resonators, *Phys. Rev. Res.* **3**, 013122 (2021).
- [40] H.-c. Kao, Chiral zero modes in superconducting nanowires with Dresselhaus spin-orbit coupling, *Phys. Rev. B* **90**, 245435 (2014).
- [41] S. Hegde, V. Shivamoggi, S. Vishveshwara, and D. Sen, Quench dynamics and parity blocking in Majorana wires, *New J. Phys.* **17**, 053036 (2015).
- [42] S. S. Hegde and S. Vishveshwara, Majorana wavefunction oscillations, fermion parity switches, and disorder in Kitaev chains, *Phys. Rev. B* **94**, 115166 (2016).
- [43] D. J. Apigo, K. Qian, C. Prodan, and E. Prodan, Topological edge modes by smart patterning, *Phys. Rev. Mater.* **2**, 124203 (2018).
- [44] K. Qian, D. J. Apigo, C. Prodan, Y. Barlas, and E. Prodan, Topology of the valley-Chern effect, *Phys. Rev. B* **98**, 155138 (2018).
- [45] K. Qian, L. Zhu, K. H. Ahn, and C. Prodan, Observation of flat frequency bands at open edges and antiphase boundary seams in topological mechanical metamaterials, *Phys. Rev. Lett.* **125**, 225501 (2020).
- [46] L. Zhu, E. Prodan, and K. H. Ahn, Flat energy bands within antiphase and twin boundaries and at open edges in topological materials, *Phys. Rev. B* **99**, 041117(R) (2019).
- [47] See Supplemental Material at <http://...> for details of the experimental setup, the typical spectra for the topological insulator, metallic, and nontopological insulator phases, theoretical ranges for bulk bands, the band gap versus  $\beta_g$  for both the experiments and the theory, details of MLBS spatial profile from the theory, and the slow motion videos of bulk modes and MLBSs for Figs. 1(g), 1(i), 2(a), 2(b), and 2(c).
- [48] M. A. Hasan, K. Runge and P. A. Deymier, Experimental classical entanglement in a 16 acoustic qubit-analogue, *Sci. Rep.* **11**, 24248 (2021).
- [49] J. Ávila, E. Prada, P. San-Jose, and R. Aguado, Majorana oscillations and parity crossings in semiconductor nanowire-based transmon qubits, *Phys. Rev. Res.* **2**, 033493 (2020).
- [50] The difference between theory and experiments for  $N=4$  system is likely originated from disorders present in the experimental setup. For example, the two theoretically predicted MLBS peaks are close enough that they could be switched in the experiments due to disorders. Possible source of the disorders includes the moments of inertia of the attached accelerometers.
- [51] J. Sau, S. Simon, S. Vishveshwara, and J. R. Williams, From anyons to Majoranas, *Nature Rev. Phys.* **2**, 667 (2020).